Geophysical Prospecting

EAGE EUROPEAN ASSOCIATION OF GEOSCIENTISTS & ENGINEERS

Geophysical Prospecting, 2011, **59**, 161–175 doi: 10.1111/j.1365-2478.2010.00899.x

Applying essentially non-oscillatory interpolation to controlled-source electromagnetic modelling*

M. Wirianto[1†], W.A. Mulder[1,2] and E.C. Slob[1]

[1]*Department of Geotechnology, Delft University of Technology, PO Box 5048, 2600 GA Delft, the Netherlands, and* [2]*Shell International E&P BV, PO Box 60, 2280 AB Rijswijk, the Netherlands*

Received October 2008, revision accepted April 2010

ABSTRACT

Modelling and inversion of controlled-source electromagnetic (CSEM) fields requires accurate interpolation of modelled results near strong resistivity contrasts. There, simple linear interpolation may produce large errors, whereas higher-order interpolation may lead to oscillatory behaviour in the interpolated result. We propose to use the essentially non-oscillatory, piecewise polynomial interpolation scheme designed for piecewise smooth functions that contains discontinuities in the function itself or in its first or higher derivatives. The scheme uses a non-linear adaptive algorithm to select a set of interpolation points that represent the smoothest part of the function among the sets of neighbouring points.

We present numerical examples to demonstrate the usefulness of the scheme. The first example shows that the essentially non-oscillatory interpolation (ENO) scheme better captures an isolated discontinuity. In the second example, we consider the case of sampling the electric field computed by a finite-volume CSEM code at a receiver location. In this example, the ENO interpolation performs quite well. However, the overall error is dominated by the discretization error. The other examples consider the comparison between sampling with essentially non-oscillatory interpolation and existing interpolation schemes. In these examples, essentially non-oscillatory interpolation provides more accurate results than standard interpolation, especially near discontinuities.

Key words: Electromagnetic modelling, Interpolation, Numerical modelling.

INTRODUCTION

The marine controlled-source electromagnetic (CSEM) method was introduced in the late 1970s to study the resistivity of the oceanic lithosphere (Cox 1981; Constable and Srnka 2007). The method was originally intended as a complement to magnetotelluric (MT) measurements to obtain data at relatively higher frequencies than present in the MT signal after travelling through sea water. As electromagnetic (EM) measurements enable a distinction between highly resistive bodies and their surrounding structures, the method attracted the attention of the oil industry because hydrocarbon reservoirs are far more resistive than brine-filled formations. As reported by many authors, controlled-source electromagnetic (CSEM) measurements may indicate the presence of hydrocarbons (Eidesmo *et al.* 2002; Ellinsgrud *et al.* 2002; Amundsen, Johnstad and Røsten 2004; Carazzone *et al.* 2005; Srnka *et al.* 2006; Choo *et al.* 2006; Darnet *et al.* 2007; MacGregor *et al.* 2007). Moreover, CSEM data and inversion results have nowadays found their use for derisking potential prospects, complementary to seismics. Comprehensive overviews can be found in,

*This paper is based on extended abstract P074 presented at the 70th EAGE Conference & Exhibition Incorporating SPE EUROPEC 2008, 9–12 June 2008 in Rome, Italy.

†E-mail: m.liam@tudelft.nl

for instance, the October 2000 issue of Inverse Problems, the March–April 2007 issue of Geophysics and the March 2007 issue of The Leading Edge.

Marine CSEM surveys typically employ a high-powered electric source close to the seafloor to induce low-frequency EM signals that penetrate into the subsurface. An array of EM receivers placed on the seafloor records the horizontal electric and magnetic field components. In many cases, the presence of hydrocarbons may be inferred by comparing the EM response to a reference data set corresponding to a background resistivity model without hydrocarbon reservoirs. However, other types of resistive structures, such as gas hydrates or anhydrite layers, may lead to false positives. In this case, full-scale inversion of the EM data for the subsurface resistivity is preferred (Plessix and Mulder 2008). This requires an accurate numerical scheme.

Various approaches for accurately solving Maxwell's equations exist. These employ a finite-difference, finite-volume, finite-element, or an integral-equation method. Each approach has its advantages and disadvantages. Finite-difference and the closely related finite-volume methods are the easiest to grasp and relatively straightforward to implement but numerical accuracy requires dense grids, affecting the memory requirements and computation time. Finite-element methods on unstructured grids allow for better gridding near sharp contrast but have a larger overhead and may result in a large sparse linear system that is more difficult to solve. For an overview of developments in numerical EM modelling, we refer to Avdeev (2005), Börner (2010) and the references listed therein.

Each method will have various sources of numerical errors that may or may not be easy to control. The numerical solution of the Maxwell equations for a general subsurface resistivity model with a finite-difference, finite-element, or finite-volume method generally involves three steps: discretization of the equations on a grid, their numerical solution and interpolation of the solution from grid points to receiver positions. Because of limitations in computational resources, each step will contribute to the numerical error in the final result. The discretization error tends to decrease with some power of the grid spacing, often with the power two for common choices that are therefore called second-order schemes. The numerical solution of the discrete equations for large-scale 3D problems is usually obtained with an iterative method as direct methods tend to be too costly. The iterative method will terminate with a residual error but with a proper algorithm, the effect on the solution will be small compared to the discretization error. Finally, the sampling of the resulting gridded solution on receiver locations will introduce an interpolation error. The subject of this paper is the accurate interpolation of the electric field components that may be discontinuous across resistivity contrasts.

We employed a finite-volume discretization of the Maxwell equations (Weiland 1977) that represent the electric field components as edge averages on the edges of a regular Cartesian, possibly stretched, grid of rectangular cells. The direction of each electric field component agrees with that of the edge it is assigned to. The discretization provides second-order accuracy for the solution if the material properties are constant (Monk and Süli 1994). When the material properties vary across the domain, the discretization, in general, leads to a first-order error in the solution (van Rienen 2001). We solved the discrete equations with BiCGSTAB2 (van der Vorst 1992; Gutknecht 1993), preconditioned by a multigrid solver (Mulder 2006). We will assume that the contribution to the numerical error of the solution method is negligible. What remains is the interpolation error that occurs when the edge averages of the electric field components are interpolated to the receiver positions. Tri-linear interpolation is the simplest approach on the grids we use. When the solution is smooth, it adds a second-order contribution to the discretization error, caused by the linear interpolation as well as the second-order difference between edge-averages and point values. Near sharp resistivity contrasts, the field component perpendicular to the interface that separates the two resistivities is discontinuous and the linear interpolation scheme may lead to large errors in this case. Since the computational cost of interpolation is much less than that of the solver, the use of a more accurate interpolation scheme appears to be worthwhile.

We want to have an interpolation scheme that can deal with edge averages as well as point values and that can handle discontinuities in the field components or their spatial derivatives. A scheme with these properties has already been devised by Harten *et al.* (1997) and named essentially non-oscillatory interpolation. The method was originally designed to improve the numerical accuracy of Godunov's scheme (Godunov 1959) for compressible flow computations with shock waves and contact discontinuities. The original Godunov scheme is a finite-volume method that represents the solution by piecewise constant values per grid cell. Time-stepping requires fluxes at the boundaries between neighbouring cells. These are determined from the exact solution of the so-called Riemann problem. Although the scheme avoids the numerical oscillations that plague central difference schemes, it is only first-order accurate. The numerical error can be interpreted as artificial diffusion, causing discontinuities to be smeared out. Van Leer

(1979) proposed a higher-order extension of the method that constructs piecewise polynomials per cell from the given cell averages in such a way that over- and undershoots during time stepping are avoided. A piecewise linear scheme, for instance, may lead to numerical oscillations if the slope inside a cell is too steep. By reducing its size, the oscillation can be avoided. The essentially non-oscillatory scheme is a further generalization that allows for numerical oscillations but requires them to be of the same size as the numerical discretization error. Shu (1998) listed applications in many different fields, as part of the discretization of the governing equations as well as a post-processing tool for interpolating solutions to a given set of points. The last option will be considered here. In this paper, we consider the application of essentially non-oscillatory interpolation to determine the electric field components at arbitrary receiver locations in the computational domain from their computed edge averages. We investigate the accuracy of this interpolation scheme in relation to the overall error of the CSEM modelling. The outline of the paper is as follows. We first list Maxwell's equations for a conducting medium and give the main steps in the numerical solution procedure, the details of which can be found elsewhere (Mulder 2006). The essentially non-oscillatory interpolation scheme is reviewed in Appendix A. We present a number of examples to illustrate its performance in CSEM applications. Finally, we summarize our conclusions.

THE METHOD

We briefly review Maxwell's equations for a conducting medium, which is assumed to be isotropic, time-invariant and arbitrarily inhomogeneous.

Let $\mathbf{x} = (x_1, x_2, x_3)$ denote the Cartesian coordinate vector and let t denote time. As usual, the x_3-axis is pointing downward. Maxwell's equations for conducting media in the presence of an electric current source $\mathbf{J}_s$ can be written as (Ward and Hohmann 1987; Jackson 1999; Griffiths 1999)

$$\partial_t \mathbf{B}(\mathbf{x}, t) + \nabla \times \mathbf{E}(\mathbf{x}, t) = 0, \tag{1}$$

$$\nabla \times \mathbf{H}(\mathbf{x}, t) - \partial_t \mathbf{D}(\mathbf{x}, t) = \mathbf{J}_c(\mathbf{x}, t) + \mathbf{J}_s(\mathbf{x}, t), \tag{2}$$

where the conduction current, $\mathbf{J}_c$, obeys Ohm's law,

$$\mathbf{J}_c(\mathbf{x}, t) = \sigma(\mathbf{x})\mathbf{E}(\mathbf{x}, t).$$

Here, $\sigma(\mathbf{x})$ is the conductivity, $\mathbf{E}(\mathbf{x}, t)$ is the electric field and $\mathbf{H}(\mathbf{x}, t)$ is the magnetic field. The electric displacement $\mathbf{D}(\mathbf{x}, t) = \epsilon(\mathbf{x})\mathbf{E}(\mathbf{x}, t)$ and the magnetic induction $\mathbf{B}(\mathbf{x}, t) = \mu(\mathbf{x})\mathbf{H}(\mathbf{x}, t)$. Parameters ϵ and μ are respectively the permittivity and the magnetic permeability. Both parameters are usually expressed as $\epsilon = \epsilon_r \epsilon_0$ and $\mu = \mu_r \mu_0$, where ϵ_r and μ_r are their relative values and ϵ_0 and μ_0 their absolute values in vacuum. Non-conductive media have an extremely small value of σ, which is idealized as $\sigma = 0$.

Using equation (1), we can eliminate the magnetic field from equation (2), yielding the second-order parabolic system of equations,

$$\mu_0 \epsilon \partial_t \partial_t \mathbf{E} + \mu_0 \sigma \partial_t \mathbf{E} + \nabla \times \mu_r^{-1} \nabla \times \mathbf{E} = -\mu_0 \partial_t \mathbf{J}_s.$$

To transform from the time domain to the frequency domain, we define the temporal Fourier transform of a space- and time-dependent vector field $\mathbf{E}(\mathbf{x}, t)$ as

$$\hat{\mathbf{E}}(\mathbf{x}, \omega) = \int_{-\infty}^{\infty} \mathbf{E}(\mathbf{x}, t) e^{\mathrm{i}\omega t}\, dt,$$

where i is the imaginary unit and ω the angular frequency. The resulting system of equations is

$$\mathrm{i}\omega\mu_0\tilde{\sigma}\hat{\mathbf{E}} - \nabla \times \mu_r^{-1} \nabla \times \hat{\mathbf{E}} = -\mathrm{i}\omega\mu_0 \hat{\mathbf{J}}_s, \tag{3}$$

where $\tilde{\sigma} = \sigma - \mathrm{i}\omega\epsilon$.

To compute a numerical solution of equation (3) for a given conductivity and source term, we discretized the equations on a stretched grid with the finite integration technique (Weiland 1977) and solved the resulting system of equations with an iterative method using a multigrid solver as a preconditioner (Mulder 2006). For an assessment of the method's performance, we refer to earlier papers (Mulder 2006, 2008; Mulder, Wirianto and Slob 2008). The method is matrix-free: we never explicitly form the large sparse linear matrix that describes the discretized problem but only evaluate its action on the latest estimate of the solution, thereby reducing storage requirements.

The discretization starts with a grid of block-shaped cells. The three electromagnetic field components are represented as average values on edges, the x-components on edges parallel to the x-direction and the y- and z-components parallel to their corresponding directions. This approach can be interpreted as a finite-volume generalization of the scheme by Yee (1966). Perfectly electric conducting boundary conditions are used where the model is truncated. To reduce the influence of these unrealistic boundary conditions on the resulting solution, we applied grid stretching to move them sufficiently far away from the region of interest.

The discretization with the finite integration technique provides a representation of the electric field components as edge averages. Since the receivers can be located at arbitrary positions relative to the computational grid, interpolation is

required. Here, we propose to use the essentially non-oscillatory interpolation scheme. Like standard Newton interpolation, essentially non-oscillatory interpolation starts with calculating a table of divided differences. Instead of selecting points symmetrically around the point where the interpolated value is needed, essentially non-oscillatory interpolation applies an adaptive algorithm, choosing a stencil – a set of subsequent points – in such a way that the resulting interpolating polynomial does not have large oscillations. If, for instance, we want to perform quadratic interpolation to a given point, we can select the nearest grid point and its left and right neighbours. Essentially non-oscillatory interpolation considers the two grid points on both sides of the given point and chooses the third grid point either to the left or to the right of the other two, preferring the choice with the smallest values of the divided differences. We refer to Appendix A for details.

EXAMPLES

We present a number of examples that highlight the difficulties related to interpolating averaged field values on a non-uniformly sampled grid for piecewise continuous fields. We first illustrate the performance of essentially non-oscillatory interpolation when reconstructing a simple function with an isolated discontinuity. We then consider the accuracy improvement provided by essentially non-oscillatory interpolation when applied to a simple electromagnetic test problem. Finally, we investigate the performance of essentially non-oscillatory interpolation in CSEM modelling of a marine configuration with a lateral discontinuity in the sea-bed.

The values of all quantities are given in SI units, except for the first test where dimensionless values are used.

Simple test problem

To illustrate the performance of essentially non-oscillatory interpolation, we first consider the reconstruction of the function $y(x) = \cos(\pi x) + \text{sign}(x - 1)$, $0 \leq x \leq 2$. We divide the interval $[0, 2]$ into N equidistant cells and define the grid points,

$$x_i = i \cdot \frac{2}{N}, \quad i = 0, 1, \ldots, N.$$

We compute cell averages and interpolate to point values at cell centres. Table 1 lists the number of cells and errors.

The error is calculated in the 2-norm and maximum norm. If the grid has N number of cells, the error in the 2-norm is defined as

$$\varepsilon_2 = \left[\sum_{i=1}^{N} (\tilde{y}_i - y_i)^2 \right]^{1/2},$$

and the relative error as

$$\varepsilon_{r;2} = \varepsilon_2 \left[\sum_{i=1}^{N} y_i^2 \right]^{-1/2},$$

where $\tilde{y}_i \equiv \tilde{y}(x_{c;i})$ denotes the numerical solution and $y_i \equiv y(x_{c;i})$ the function values, calculated at cell centres $x_{c;i} = (x_i + x_{i-1})/2$. For the maximum norm, we have

$$\varepsilon_\infty = \max_{i=1,\ldots,N} |\tilde{y}_i - y_i|,$$

and the relative error is

$$\varepsilon_{r;\infty} = \varepsilon_\infty \left[\max_{i=1,\ldots,N} |y_i| \right]^{-1}.$$

Table 1 lists the relative errors for various numbers of cells, given by N. Figure 1 shows the result of cubic essentially non-oscillatory interpolation when N is set to 40. When compared to standard cubic-spline interpolation, we clearly see that the essentially non-oscillatory scheme better captures the discontinuity.

Table 1 Solution error for a function reconstruction test problem with an increasing numbers of cells, N. The relative errors $\varepsilon_{r;2}$ and $\varepsilon_{r;\infty}$ were obtained with cubic essentially non-oscillatory interpolation (essentially non-oscillatory$_3$) or with standard cubic-spline interpolation

	$\varepsilon_{r;2}$ - ERROR		$\varepsilon_{r;\infty}$ - ERROR	
N	essentially non-oscillatory$_3$	Spline	essentially non-oscillatory$_3$	Spline
20	0.115×10^{-5}	0.105	0.156×10^{-5}	0.201
40	0.579×10^{-7}	0.074	0.109×10^{-6}	0.200
80	0.273×10^{-8}	0.053	0.697×10^{-8}	0.200
160	0.129×10^{-9}	0.037	0.439×10^{-9}	0.200

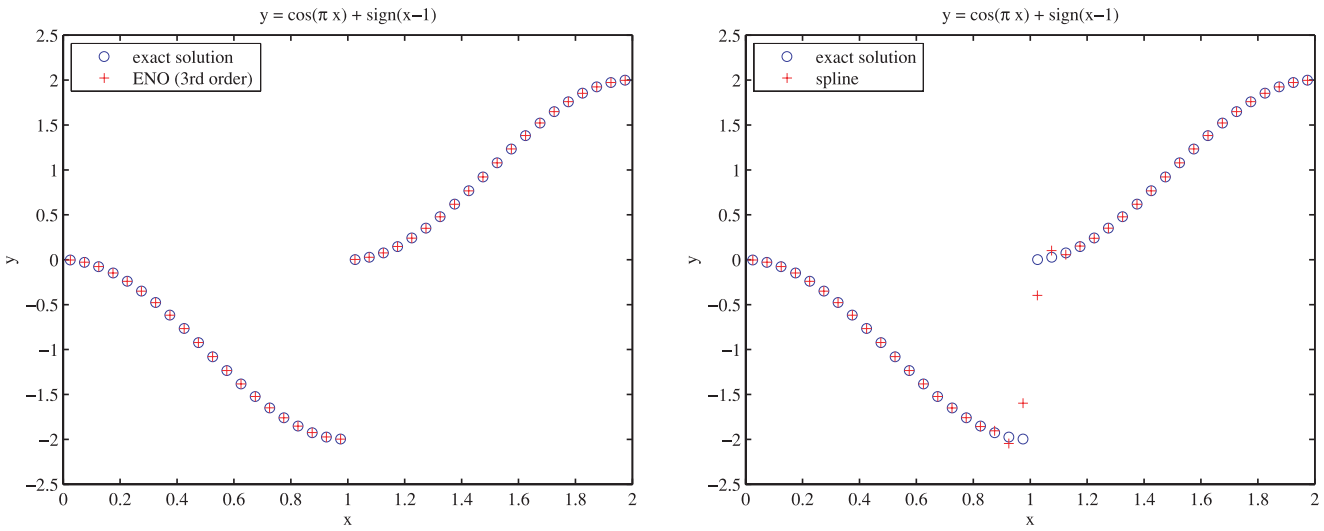

Figure 1 Result for the cubic essentially non-oscillatory interpolation scheme (left) and for standard cubic-spline interpolation (right) of a function with an isolated discontinuity.

Artificial test problem

The finite-volume multigrid solver provides the solution of the EM problem as edge-averaged components of the electric field, where the coordinate direction of the component agrees with the direction of the edge. We can apply essentially non-oscillatory interpolation to map the edge averages to point values. Here, we investigate the accuracy of the interpolation scheme.

We repeated the artificial test problem of Mulder (2008). It is based on eigenfunctions that obey the perfectly electric conducting boundary conditions. We consider a domain $\Omega = [0, 2\pi]^3$ m^3 and split it into two parts, Ω_1 with $z < \pi$ and Ω_2 for $z > \pi$. The conductivity $\sigma = 10 + (x + 1)(y + 2)(z - \pi)^2$ S/m in Ω_1 and $\sigma = 10$ S/m in Ω_2. We set $\epsilon_r = 0$, which is unphysical, $\mu_r = 1$, and $\omega = 10^6$ rad/s. We define the exact solution as

$$E_1 = -2\partial_x\psi, \quad E_2 = -2\partial_y\psi, \quad E_3 = \partial_z\psi,$$

where $\psi = \sin x \cdot \sin y \cdot \sin z$. We computed edge averages of the current source, $\mathbf{J}_s = -\tilde{\sigma}\mathbf{E} + \nabla \times (\mathrm{i}\omega\mu)^{-1}\nabla \times \mathbf{E}$, by integrating the substituted exact solution.

Table 2 lists the errors in the numerical solution after interpolation of the edge averages of the three electric field components to point values at the midpoints of the edges where the components are assumed to live. The first component, E_1, is represented on edges parallel to the x-direction, E_2 lives on midpoints of edges parallel to the y-direction and E_3 on edges parallel to z. The errors were measured by the 2-norm and the maximum norm, using the same definitions as Mulder (2008). The norms are measuring the difference

Table 2 Solution errors for the artificial test problem with an increasing number, $N \times N \times N$, of cells. The relative errors $\varepsilon_{r;2}$ and $\varepsilon_{r;\infty}$ were obtained with standard cubic-spline interpolation applied to the numerical solution (superscript n), with cubic essentially non-oscillatory interpolation (essentially non-oscillatory$_3$) applied to the numerical solution (superscript ne) or the exact solution (superscript ee)

		L_2 - ERROR			L_∞ - ERROR		
N	$h_{\max}$	$\varepsilon^n_{r;2}/h^2_{\max}$	$\varepsilon^{ne}_{r;2}/h^2_{\max}$	$\varepsilon^{ee}_{r;2}/h^4_{\max}$	$\varepsilon^n_{r;\infty}/h^2_{\max}$	$\varepsilon^{ne}_{r;\infty}/h^2_{\max}$	$\varepsilon^{ee}_{r;\infty}/h^4_{\max}$
16	0.39	$8.6 \cdot 10^{-2}$	$7.5 \cdot 10^{-2}$	$1.5 \cdot 10^{-2}$	0.21	0.19	0.03
32	0.20	$8.8 \cdot 10^{-2}$	$7.7 \cdot 10^{-2}$	$1.3 \cdot 10^{-2}$	0.24	0.21	0.04
64	0.098	$8.9 \cdot 10^{-2}$	$7.8 \cdot 10^{-2}$	$1.0 \cdot 10^{-2}$	0.24	0.22	0.04
128	0.049	$8.9 \cdot 10^{-2}$	$7.8 \cdot 10^{-2}$	$0.8 \cdot 10^{-2}$	0.24	0.22	0.04

between the numerical value and the exact value at the grid points. Since the numerical values are obtained as edge averages, we used the essentially non-oscillatory interpolation to map it to the point values at the same grid points. The number of cells in each coordinate direction is given by $N_x = N_y = N_z = N$. We compared the error in the numerical solution with cubic spline (superscript *n*) interpolation and with essentially non-oscillatory (superscript *ne*) interpolation. To distinguish between the contribution of the discretization error and the interpolation error, we also applied essentially non-oscillatory interpolation to the exact solution, represented in the form of edge averages. The results in Table 2 are marked by the superscript *ee*.

The discretization scheme in our modelling code leads to a solution with second-order accuracy, confirmed by the observed $\varepsilon^n_{r;2}$ and $\varepsilon^n_{r;\infty}$ in Table 2. The errors were divided by the square of the largest cell width $h_{\max}$, which is the maximum value over all the cell widths in the three coordinate directions. The results in Table 2 show that the essentially non-oscillatory interpolation reduces the overall errors, compared to standard cubic-spline interpolation, although the results are still second-order accurate. If we compare this to the result of essentially non-oscillatory interpolation on the exact solution marked by the superscript *ee* and which is normalized to $h^4_{\max}$, we can conclude that the main contribution to the error is due to the numerical discretization. Here, we used cubic essentially non-oscillatory interpolation. The resulting interpolation errors reduce proportional to the fourth power of the step size, provided exact function values are given on the original grid.

We also investigated the effect of essentially non-oscillatory interpolation when grid stretching was applied. The grid stretching is carried out in such a way that the ratio between neighbouring cell widths in each direction is $1 + \alpha$ when marching away from the origin. An equidistant grid is obtained for $\alpha = 0$. Table 3 lists the result for grid stretching with $\alpha = 0.04$. Similarly to the results without grid stretching in Table 2, the error is mainly caused by the numerical discretization.

In these examples, we observe that the interpolation error is small relative to the second-order numerical discretisation error. Still, essentially non-oscillatory interpolation provides some improvement over standard cubic-spline interpolation.

Layered models with current source

The computational cost of the multigrid solver is typically of $O(N^3)$, meaning that the cost increases 8 times when the number of grid cells N in each coordinate direction is doubled or the cell width is halved. For large-scale problems that require a relatively fine grid to accurately capture the solution, the cubic scaling with grid spacing may be an issue. Because the interpolation scheme is much cheaper than solving the equations on a finer grid, essentially non-oscillatory interpolation may be useful. To assess the potential usefulness of essentially non-oscillatory interpolation for obtaining the electric field at the receiver positions, we compared the result of essentially non-oscillatory interpolation for a solution with a certain grid sampling to the result obtained by standard linear interpolation on a grid with a finer sampling.

For this comparison, we considered a homogeneous halfspace with a conductivity σ of 0.5 S/m for $z \geq 0$ and zero elsewhere. A point dipole-source in the x-direction was placed at the surface. The frequency was set to 1 Hz. We computed the electric field with the multigrid solver on two different grids, containing either 128^3 or 256^3 cells. Both required five BiCGStab iterations to have the residual drop to 10^{-7} of its original value. This took about 35 minutes for the grid with 128^3 cells and 6 hours for the one with 256^3 cells. Next, we applied the cubic ENO interpolation and the standard linear interpolation scheme. Figure 2 shows the amplitude-versus-offset behaviour of the in-line electric field, plotted together with its numerical error. Figure 2 confirms that the code provides a reasonably accurate solution, particularly for offsets larger than 100 m. The large error for the near-field is due

Table 3 As Table 2 but for a stretched grid

		L_2 - ERROR			L_∞ - ERROR		
N	$h_{\max}$	$\varepsilon^n_{r;2}/h^2_{\max}$	$\varepsilon^{ne}_{r;2}/h^2_{\max}$	$\varepsilon^{ee}_{r;2}/h^4_{\max}$	$\varepsilon^n_{r;\infty}/h^2_{\max}$	$\varepsilon^{ne}_{r;\infty}/h^2_{\max}$	$\varepsilon^{ee}_{r;\infty}/h^4_{\max}$
16	0.45	$8.2 \cdot 10^{-2}$	$7.0 \cdot 10^{-2}$	$1.3 \cdot 10^{-2}$	0.18	0.16	0.03
32	0.26	$8.0 \cdot 10^{-2}$	$6.9 \cdot 10^{-2}$	$1.3 \cdot 10^{-2}$	0.16	0.14	0.03
64	0.17	$7.4 \cdot 10^{-2}$	$6.6 \cdot 10^{-2}$	$1.1 \cdot 10^{-2}$	0.15	0.13	0.03
128	0.13	$6.9 \cdot 10^{-2}$	$6.3 \cdot 10^{-2}$	$0.8 \cdot 10^{-2}$	0.14	0.13	0.04

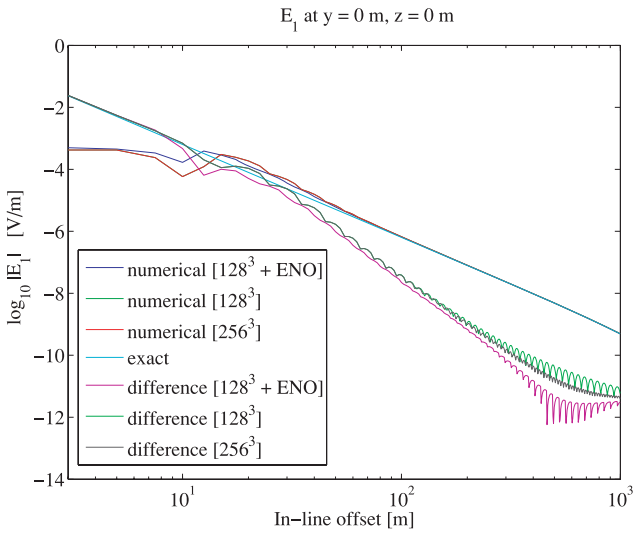

Figure 2 In-line electric field component computed on two different grids. The numerical solutions match the exact solution, except close to the source. The difference between the numerical and exact solutions is smallest with cubic essentially non-oscillatory interpolation.

to the source modelling. To represent the point source on the grid, we used a Gaussian distribution of small width, centred at the source position. The standard deviation was set to 0.5 m. We interpolated the solution to the 400 points used in the graph by standard linear interpolation and also by essentially non-oscillatory interpolation on the solution obtained for the 128^3 grid cells.

In the example, the same interpolation scheme applied to the solution on the finer grid results in a smaller error than obtained for the coarser grid, particularly at the far offsets where the grid spacing differed significantly between the coarse and fine grid. We also find that the essentially non-oscillatory interpolation on the solution obtained for 128^3 cells produces a more accurate result than the standard linear interpolation applied to the solution on 256^3 cells. Given the relatively low computational cost of the essentially non-oscillatory interpolation, the usefulness of the method is clear.

The next example is a three-layer problem. We considered the performance of the essentially non-oscillatory interpolation in a simple geophysical configuration with air, water and sediments. The layers have a conductivity σ of 0, 3 and 0.5 S/m, respectively and a relative permittivity ϵ_r of 1, 80 and 17. The water depth is 200 m. A dipole source in the x-direction is located at a depth of 175 m. The frequency is set to 0.5 Hz.

Here, we focus on the vertical electric field component along a vertical line because this component has discontinuities at the interfaces that separate two different resistivities and the essentially non-oscillatory interpolation can be used to capture the discontinuities. Since we would like to avoid the error that comes from the numerical method, we used the exact solution. We first define an equidistant grid along the z-direction with a grid sampling of 10 m. The grid sampling is set in such a way that the interface of the discontinuity coincides with a grid point. We derived the exact solution, given in Appendix B, by solving Maxwell's equations in the wave number domain and then taking the inverse Fourier transform to go back to the spatial domain (Ward and Hohmann 1987).

Figure 3 shows the comparison. We plot the vertical electrical field component along a vertical line at position

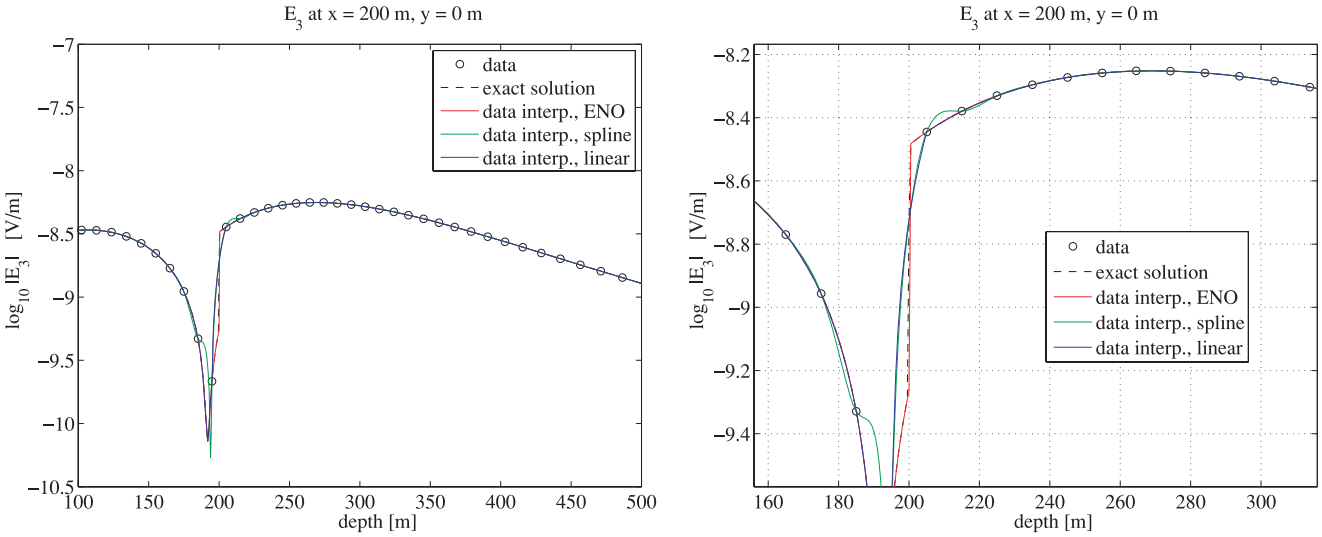

Figure 3 The vertical electric field component at $x = 200$ m and $y = 0$ m. The right panel shows an enlargement around the discontinuity.

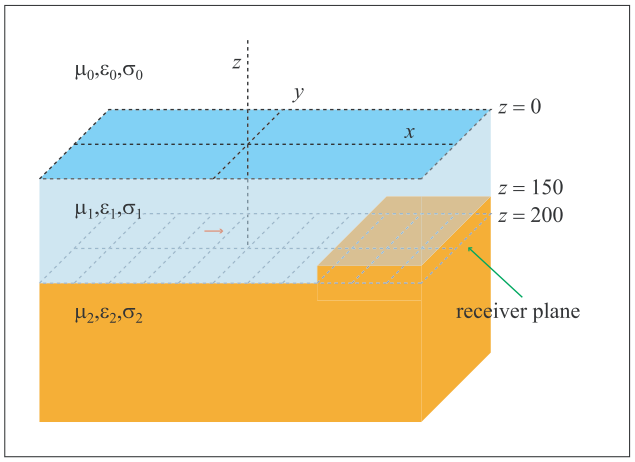

Figure 4 A three-layer configuration with air, sea-water, and sediments and simple bathymetry.

$x = 200$ m and $y = 0$ m. In the figure, we can see clearly that the vertical electrical field component has a discontinuity exactly at $z = 200$ m, the depth of the interface between the water and sediment layer. The zoomed figure in the right panel shows that the essentially non-oscillatory interpolation captures the discontinuity quite well, whereas the standard cubic-spline interpolation produces an oscillation. The error also appears when we use the standard linear interpolation.

Modified three-layer problems

In the previous example, the material discontinuities matched grid lines so they could be accurately represented in the numerical scheme. Essentially non-oscillatory interpolation then helps to capture the discontinuities in the solution. In general, the discontinuities will not be aligned with the lines of a Cartesian grid. The projection of the material properties onto the grid will then require some averaging. The averaging will affect the numerical solution. We investigate this case next. The previous three-layer problem is modified by having an abrupt change in water depth following a grid line. The numerical solution and interpolation results are then compared to the same problem where the grid is rotated relative to the model, so that the jump in water depth does not follow a grid line.

We added a simple bathymetry model to the previous three-layer problem by setting the water depth at either 200 m or 150 m with a jump at $x = 250$ m from deeper to shallower water when x increases (see Fig. 4). A dipole source in the x-direction was positioned at a depth of 175 m and at a 250 m distance from the jump in the water depth. We used the same frequency as before. An array of receivers was located at a depth of 200 m. We defined the grid points in such a way that the interface of the jump coincided with the grid lines (see the left panel of Fig. 5). We will refer to this model as the regular configuration. Secondly, we used the same configuration but rotated the grid lines by 30 degrees so that the interface of the jump no longer coincided with the grid lines (see the right-hand panel of Fig. 5). The rotation centre is at the source location. We will call this the rotated configuration.

We computed the numerical solution for the regular configuration with the multigrid solver containing 128^3 cells, with cell widths varying from 25 m to about 5 km and interpolated the result to the receiver locations with cubic essentially non-oscillatory interpolation. Figure 6 shows the result at a depth of 200 m. As expected, the cubic essentially non-oscillatory interpolation captures the discontinuity at the in-line distance of 250 m quite well. Further on, we will use this result as a reference to make a comparison between different interpolation methods.

We repeated the computations for the rotated configuration and interpolated the results to the same receiver locations as before. Figure 7 shows the result at a depth of 200 m for tri-linear and Fig. 8 for cubic essentially non-oscillatory interpolation. The difference between the solutions on the regular, aligned grid and the rotated one is indicative of the numerical error in the solution. The largest difference occurs near the discontinuity, where the tri-linear nor the cubic essentially non-oscillatory interpolation can recover the jump in the solution. On the rotated grid, the jump is actually smoothed. In our modelling, the material parameters are assumed to be given as averages per cell. The projection of the original model to the rotated grid introduces some smoothing when computing these cell averages. This, in turn, causes the solution to be smoothed. Essentially non-oscillatory interpolation cannot remove this smoothing when used as a post-processing operation and hardly performs better than tri-linear interpolation in this case. Comparing Figs 7 and 8, we observe that the tri-linear interpolation produces a difference that is more oscillatory than obtained with the cubic essentially non-oscillatory interpolant. This is due to the fact that the latter, which was also used for the reference curve, introduces more small-scale details than tri-linear interpolation.

CONCLUSIONS

The computation of accurate solutions to CSEM problems requires an accurate discretization, a robust solver and an accurate interpolation scheme to sample the numerical solution at receiver locations. We used a numerical scheme that

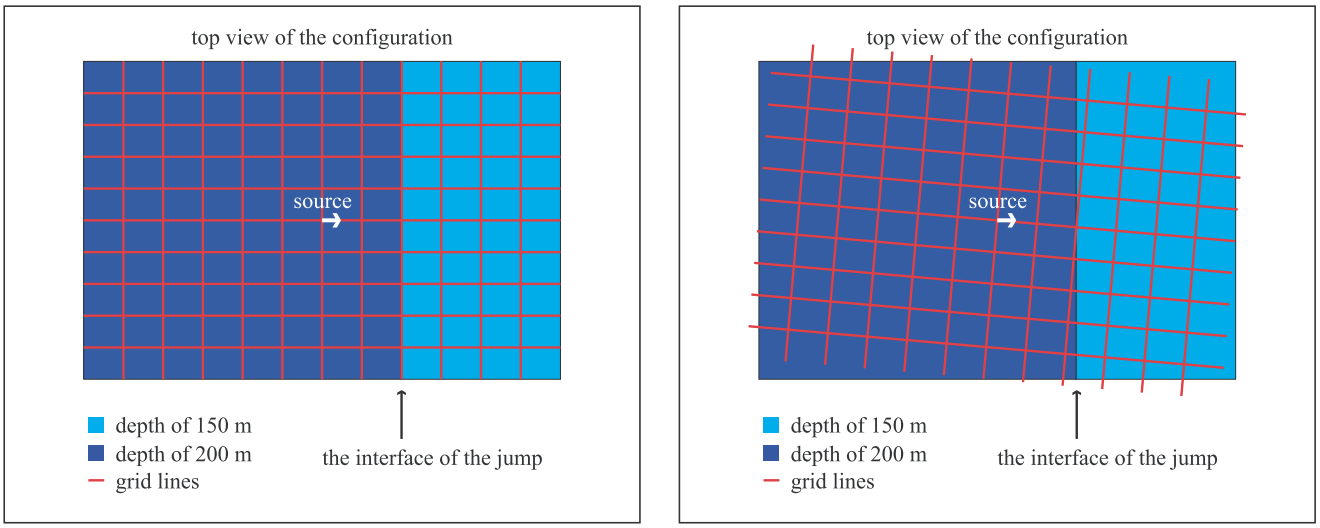

Figure 5 The left panel shows a top view of a configuration where the grid is aligned with the jump in the sea-bottom depth. The alignment is lost when the grid is rotated, as shown in the right panel.

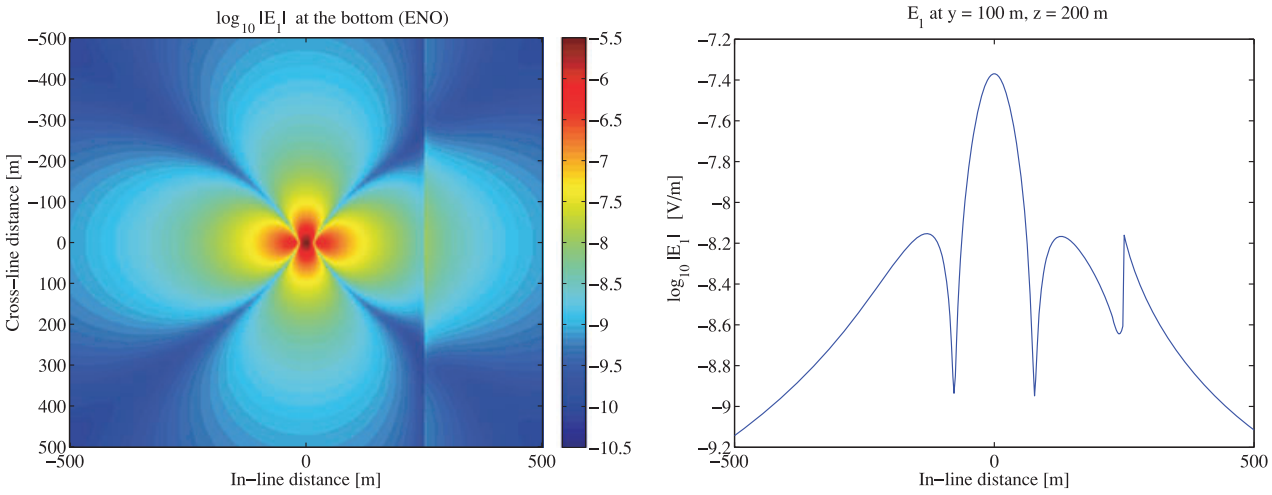

Figure 6 The in-line electric field component at a depth of 200 m obtained with the aligned grid. The right panel shows the values along $y = 100$ m. Of course, sea bottom receivers can only be found for an in-line distance less than 250 m.

provides the numerical solution as edge averages of the electric field components, each component living on the edges of cells that are parallel to the component's orientation. The interpolation of the edge averages of the possibly discontinuous field components to receiver positions was carried out with the essentially non-oscillatory interpolation scheme, because this method can handle edge averages as well as discontinuities in the solution or derivatives of the solution.

Comparison to standard tri-linear or cubic interpolation shows that essentially non-oscillatory interpolation provides more accurate results near discontinuities. Still, in the examples considered here, the discretization error tends to dominate the final result and essentially non-oscillatory interpolation only gives a moderate improvement. Given its low cost, it still appears to be worthwhile to use the scheme.

ACKNOWLEDGMENTS

Marwan Wirianto received financial support from the sponsors of the Delphi consortium. The authors thank Ali M. Tehrani (Delft University of Technology) for his help in the comparison of the three-layer problem.

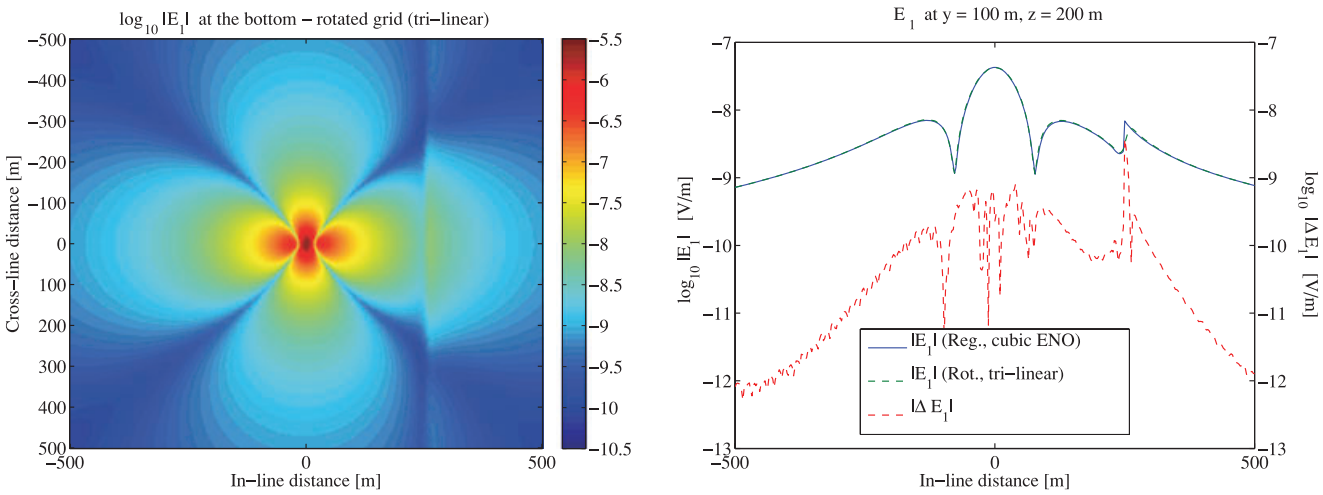

Figure 7 The left panel shows the in-line electric field component at a depth of 200 m in the rotated configuration using standard tri-linear interpolation. The right panel compares values along $y = 100$ m. The solid blue line is the result of cubic ENO interpolation in the regular configuration, whereas the dashed green line was obtained with tri-linear interpolation in the rotated configuration. The dashed red line shows the differences between the two. The abbreviation 'Rot.' refers to the rotated configuration and 'Reg.' to the regular configuration. The differences are relatively small, except close to the discontinuity.

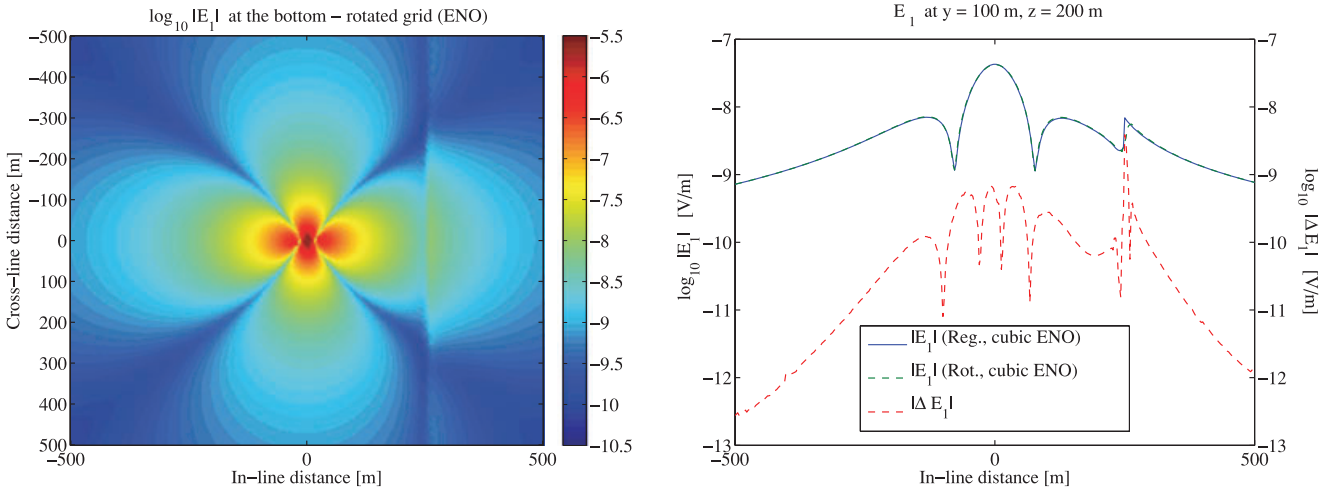

Figure 8 As Fig. 7, but for cubic ENO interpolation.

REFERENCES

Amundsen H.E.F., Johnstad S.E. and Røsten T. 2004. A sea bed logging (SBL) calibration survey over the Troll gas field. 66th EAGE meeting, Paris, France, Expanded Abstracts, E019.

Avdeev D.B. 2005. Three-dimensional electromagnetic modelling and inversion from theory to application. *Surveys in Geophysics* **26**, 767–799.

Börner R.-U. 2010. Numerical modelling in geo-electromagnetics: Advances and challenges. *Surveys in Geophysics* **31**, 225–245.

Carazzone J.J., Burtz O.M., Green K.E., Pavlov D.A. and Xia C. 2005. Three dimensional imaging of marine CSEM data. *SEG Technical Program Expanded Abstracts* **24**, 575–578.

Choo C.K., Rosenquist M., Rollett E., Ghaffar, Kamal. A.Abd., Voon J. and Wong H.F. 2006. Detecting hydrocarbon reservoir with SeaBed Logging in deepwater Sabah, Malaysia. *SEG Technical Program Expanded Abstracts* **25**, 714–718.

Constable S. and Srnka L.J. 2007. An introduction to marine controlled-source electromagnetic methods for hydrocarbon exploration. *Geophysics* **72**, WA3–WA12.

Cox C.S. 1981. On the electrical conductivity of the oceanic lithosphere, *Physics of the Earth and Planetary Interiors* **25**, 196–201.

Darnet M., Choo M.C.K., Plessix R.-E., Rosenquist M.L., Yip-Cheong K., Sims E. and Voon J.W.K. 2007. Detecting hydrocarbon reservoirs from CSEM data in complex settings: Application to deepwater Sabah, Malaysia. *Geophysics* **72**, WA97–WA103.

Eidesmo T., Ellinsgrud S., MacGregor L.M., Constable S., Sinha M.C., Johansen S., Kong F.N. and Westerdahl H. 2002. Sea Bed Logging (SBL), a new method for remote and direct identification of hydrocarbon filled layers in deepwater areas. *First Break* **20**, 144–152.

Ellinsgrud S., Eidesmo T., Johansen S., Sinha M.C. and MacGregor L.M., 2002. Remote sensing of hydrocarbon layers by seabed logging (SBL): Results from a cruise offshore Angola. *The Leading Edge* **21**, 972–982.

Godunov S.K. 1959. A difference scheme for numerical solution of discontinuous solution of hydrodynamic equations. *Mat. Sbornik* **47**, 271–306. Translated US Joint Publ. Res. Service, JPRS 7226, 1969.

Griffiths D.J. 1999. *Introduction to Electrodynamics*. Prentice Hall.

Gutknecht H.H. 1993. Variants of BiCGStab for matrices with complex spectrum. *SIAM Journal on Scientific and Statistical Computing* **14**, 1020–1033.

Harten A., Osher S., Enquist B. and Chakravarthy S.R. 1986. Some results on uniformly high-order accurate essentially non-oscillatory schemes. *Journal of Applied Numerical Mathematics* **2**, 347–377.

Harten A., Enquist B., Osher S. and Chakravarthy S.R. 1997. Uniformly high order accurate essentially non-oscillatory schemes, III. *Journal of Computational Physics* **131**, 3–47.

Jackson J.D. 1999. *Classical Electrodynamics,* 3rd edn. John Wiley & Sons.

MacGregor L.M., Barker N., Overton A., Moody S. and Bodecott D. 2007. Derisking exploration prospects using integrated seismic and electromagnetic data – A Falkland Islands case study. *The Leading Egde* **26**, 356–359.

Monk P. and Süli E. 1994. A convergence analysis of Yee's scheme on nonuniform grids. *SIAM Journal on Numerical Analysis* **31**, 393–412.

Mulder W.A. 2006. A multigrid solver for 3D electromagnetic diffusion, *Geophysical Prospecting* **54**, 633–649.

Mulder W.A. 2008. Geophysical modelling of 3D electromagnetic diffusion with multigrid. *Computing and Visualization in Science* **11**, 129–138.

Mulder W.A. and van Leer B. 1985. Experiments with implicit upwind methods for the Euler equations. *Journal of Computational Physics* **59**, 232–246.

Mulder W.A., Wirianto M. and Slob E.C. 2008. Time-domain modeling of electromagnetic diffusion with a frequency-domain code. *Geophysics* **73**, F1–F8.

Plessix R-E. and Mulder W.A. 2008. Resistivity imaging with controlled-source electromagnetic data: depth and data weighting. *Inverse Problems* **24**, 034012.

Shu C.-W. 1998. Essentially non-oscillatory and weighted essentially non-oscillatory schemes for hyperbolic conservation laws. In: *Advanced Numerical Approximation of Nonlinear Hyperbolic Equations* (ed. A. Quarteroni), pp. 325–432. Springer.

Srnka L.J., Carazzone J.J., Eriksen E.A. and Ephron M.S. 2006. Remote reservoir resistivity mapping. *The Leading Egde* **25**, 972–975.

van Albada G.D., van Leer B. and Roberts W.W. 1982. A comparative study of computational methods in cosmic gas dynamics. *Astronomy and Astrophysics* **108**, 76–84.

van der Vorst H.A. 1992. Bi-CGSTAB: a fast and smoothly converging variant of Bi-CG for the solution of non-symmetric linear systems. *SIAM Journal on Scientific and Statistical Computing* **13**, 631–644.

van Leer B. 1979. Towards the ultimate conservative difference scheme. V. A second-order sequel to Godunov's method. *Journal of Computational Physics* **32**, 101–136.

van Rienen U. 2001. Frequency domain analysis of waveguides and resonators with fit on non-orthogonal triangular grids. *Progress in Electromagnetics Research (PIER)* **32**, 357–381.

Ward S.A. and Hohmann G.W. 1987. Electromagnetic theory for geophysical applications. In: *Electromagnetic Methods in Applied Geophysics – Theory, Vol. 1* (ed. M.N. Nabighian), pp. 131–311. SEG.

Weiland T. 1977. A discretization method for the solution of Maxwell's equations for six-components fields. *Electronics and Communications* **31**, 116–120.

Yee K. 1966. Numerical solution of initial boundary value problems involving Maxwell's equations in isotropic media. *IEEE Transactions on Antennas and Propagation* **16**, 302–307.

APPENDIX A: ONE-DIMENSIONAL ESSENTIALLY NON-OSCILLATORY SCHEME

When computing a numerical solution for modelling 3D CSEM, or other problems, we have to discretize the equations on a grid. If we then want to sample computed field quantities at specific receiver locations, we need some kind of interpolation procedure. In many cases, it is sufficient to use a polynomial interpolation scheme.

The polynomial interpolation schemes that are widely used in applications are usually based on a fixed stencil. For instance, to obtain an interpolation result in cell i with third-order accuracy, we can use information in the three cells $i-1$, i and $i+1$ to construct a local quadratic polynomial, except of course if cell i is located next to the boundary. This schemes works well for globally smooth solutions. However, when we apply this scheme for functions that have discontinuities, the fixed-stencil interpolation of second- or higher-order accuracy creates numerical oscillations near the discontinuities. This is referred to as the Gibbs phenomenon and is illustrated in Fig. A1 on the left side.

Essentially non-oscillatory interpolation is a higher-order interpolation scheme designed for piecewise smooth functions that contain discontinuities or have discontinuous first or higher derivatives. The scheme was originally proposed for compressible flow computations with shock waves and contact discontinuities and expanded on the earlier breakthrough work of van Leer (1979). Here we review the essentially non-oscillatory scheme for reconstructing a function in one-dimensional space.

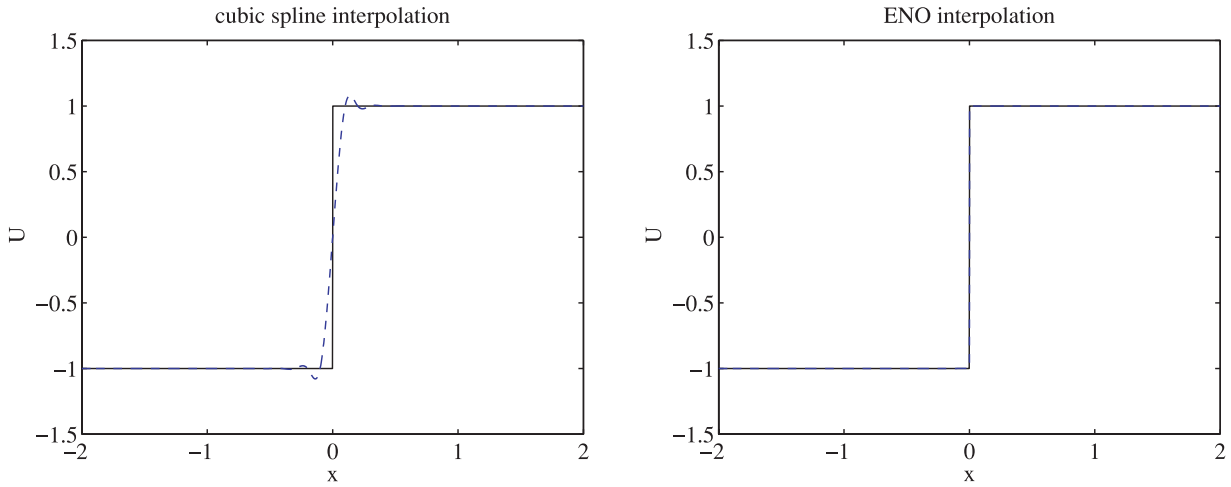

Figure A1 Cubic-spline interpolation with a fixed, centred stencil (*left*) and essentially non-oscillatory cubic interpolation (*right*) for the sign function. Solid: exact function; dashed: interpolating polynomials.

Suppose we are given a set of $N + 1$ points

$$(x_0, U_0), \quad (x_1, U_1), \quad \ldots, \quad (x_N, U_N),$$

where U_i defines the value of a piecewise smooth function $U(x)$ at a point x_i, $i = 0, 1, \ldots, N$. We define cells, cell centres and cell sizes, respectively, by

$$I_i := [x_i, x_{i+1}], \quad x_{i+\frac{1}{2}} := \frac{1}{2}(x_i + x_{i+1}),$$

and

$$\Delta x_i = x_{i+1} - x_i, \quad \text{for } i = 0, 1, \ldots, N-1.$$

Here we assume no two x_i are the same and that $\{x_i\}$ is properly ordered.

For a fixed value m, we want to reconstruct the function U by finding $H_m(x)$, a piecewise polynomial function of x with uniform polynomial degree m that satisfies the following requirements:

(i) For h sufficiently small value, $H_m(x)$ approximates the function U to $O(h^{m+1})$:

$$H_m(x) = U(x) + O(h^{m+1}),$$

at all points x for which there is a neighbourhood where U is smooth.

(ii) It is essentially non-oscillatory:

$$TV(H_m) \leq TV(U) + O(h^{m+1}), \tag{A1}$$

where TV denotes the total variation in x.

The inequality (equation A1) above ensures that the function H_m does not have spurious oscillations at a point of discontinuity. In the next paragraph we explain how to reconstruct the function H_m. The details and analysis of the reconstruction procedure can be found in Harten *et al.* (1986, 1997).

The function H_m is reconstructed as follows:

$$H_m(x_i) := U_i, \quad \text{for } i = 0, 1, \ldots N,$$

and

$$H_m(x) := p_{m,i+\frac{1}{2}}(x), \quad \text{for } x \in I_i,$$

where $p_{m,i+\frac{1}{2}}$ is a polynomial function in x of degree m. The half index $i + \frac{1}{2}$ is used to indicate that the local polynomial $p_{m,i+\frac{1}{2}}$ lives in interval I_i.

The local polynomial $p_{m,i+\frac{1}{2}}$ is obtained using Newton interpolation at $(m + 1)$ points that include x_i and x_{i+1}. Clearly, there are many possibilities for $p_{m,i+\frac{1}{2}}$ since there are many combinations of $(m + 1)$ points that include x_i and x_{i+1}. In order to reduce the number of choices and to make the numerical implementation easier, we set $p_{m,i+\frac{1}{2}}$ to be a polynomial that only passes through a stencil of $(m + 1)$ successive points. This choice implies that we obtain exactly m candidates $p_{m,i+\frac{1}{2}}$ corresponding to m different stencils of $(m + 1)$ successive points. For example, to construct an interpolating polynomial with second-order accuracy, we can use information of three points, either $\{x_{i-1}, x_i, x_{i+1}\}$ or $\{x_i, x_{i+1}, x_{i+2}\}$. Then, it only remains to choose which stencil would give the best approximation function $p_{m,i+\frac{1}{2}}$ on the interval I_i in terms of obtaining the smoothest or least oscillatory polynomial.

The information about smoothness of the polynomial is extracted from the table of divided differences, which is defined recursively by:

$$D[x_i] := U_i,$$

and

$$D[x_i, \ldots, x_{i+k}] := \frac{D[x_{i+1}, \ldots, x_{i+k}] - D[x_i, \ldots, x_{i+k-1}]}{x_{i+k} - x_i}.$$

The divided differences themselves can be viewed as approximations to first and higher derivatives of function U. How we choose a stencil of $(m + 1)$ points for which $p_{m,i+\frac{1}{2}}$ is smoothest, is basically the same problem as finding the interval where U has the smallest divided differences.

Harten *et al.* (1997) proposed a non-linear adaptive algorithm to choose a stencil of $(m + 1)$ points. Figure A2 illustrates how the algorithm works for 1D interpolation. We start by setting an initial stencil in the interval $[x_i, x_{i+1}]$, which corresponds to a $p_{1,i+\frac{1}{2}}$ that is a first-degree (linear) polynomial. We proceed to obtain a second-degree interpolant by adding to the current interval either one cell to the left

$$[x_{i-1}, x_i] \cup [x_i, x_{i+1}],$$

or one cell to the right

$$[x_i, x_{i+1}] \cup [x_{i+1}, x_{i+2}].$$

The choice is based on the absolute values of the divided differences. If,

$$|D[x_{i-1}, x_i, x_{i+1}]| < |D[x_i, x_{i+1}, x_{i+2}]|,$$

we select the interval $[x_{i-1}, x_{i+1}]$ as the next stencil, otherwise we choose the interval $[x_i, x_{i+2}]$. This procedure is repeated for larger stencils and higher-degree polynomials. Let us assume that we already have a stencil of $k + 1$ points that corresponds to the k-th degree smoothest polynomial at cell I_i,

$$[x_{j_i}, x_{j_i+k}], \quad \text{for some } j_i.$$

Then, to obtain the $(k + 1)$-th degree smoothest polynomial at cell I_i, we proceed by adding to the interval $[x_{j_i}, x_{j_i+k}]$ either one cell to the left,

$$[x_{j_i-1}, x_{j_i}] \cup [x_{j_i}, x_{j_i+k}],$$

or one cell to the right

$$[x_{j_i}, x_{j_i+k}] \cup [x_{j_i+k}, x_{j_i+k+1}].$$

The choice is based on the absolute values of $D[x_{j_i-1}, \ldots, x_{j_i+k}]$ and $D[x_{j_i}, \ldots, x_{j_i+k+1}]$. If,

$$\left|D[x_{j_i-1}, \ldots, x_{j_i+k}]\right| < \left|D[x_{j_i}, \ldots, x_{j_i+k+1}]\right|,$$

we select the interval $[x_{j_i-1}, x_{j_i+k}]$ as the next stencil, otherwise we choose the interval $[x_{j_i}, x_{j_i+k+1}]$.

We can generalize the essentially non-oscillatory interpolation to multi-dimensional spaces by repeating the one-dimensional procedure above. However, we cannot directly use the approach in our 3D CSEM modelling code, because the electric field values are computed as edge averages, whereas the essentially non-oscillatory scheme outlined in the previous section acts on point values. For edge averages, we have to consider the primitive function.

Given cell averages $\overline{u}_{i+\frac{1}{2}}$ of a piecewise smooth function $u(x)$ at the centre of each cell,

$$\overline{u}_{i+\frac{1}{2}} = \overline{u}(x_{i+\frac{1}{2}}) := \frac{1}{\Delta x_i} \int_{x_i}^{x_{i+1}} u(x)\, dx, \text{ for } i = 0, 1, \ldots, N-1.$$

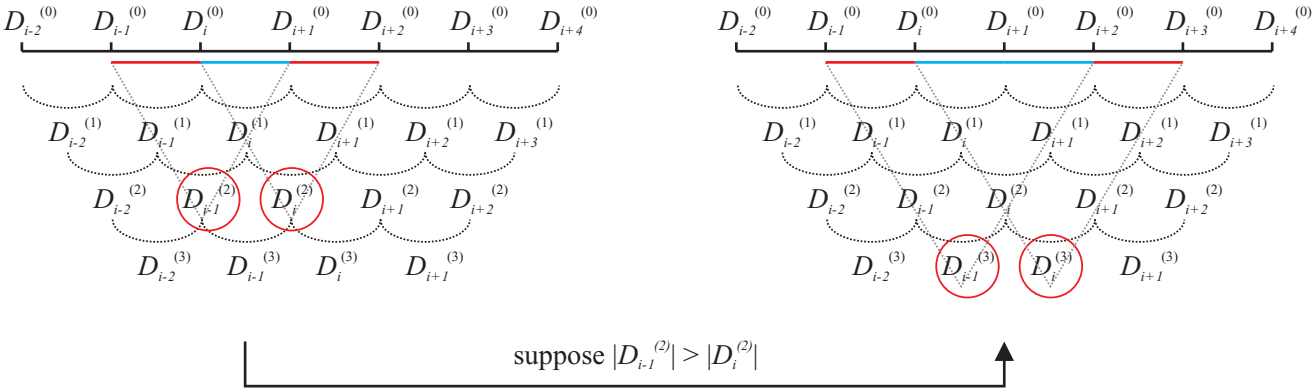

Figure A2 The essentially non-oscillatory scheme adaptively determines a stencil for interpolation by selecting the smallest divided differences. Here, we use $D_i^{(k)} \equiv D[x_i, \ldots, x_{i+k}]$ for brevity.

we can evaluate the point values of the primitive function, $U(x) = \int_{x_0}^{x} u(s)\,ds$, by

$$U(x_i) = \sum_{k=0}^{i} \overline{u}_{k+\frac{1}{2}} \Delta_{k+\frac{1}{2}}.$$

The lower bound x_0 can be chosen arbitrary. Since $u = dU/dx$, we can apply essentially non-oscillatory interpolation to the point values of the primitive function U and then obtain an approximation to u, $r(x)$, by defining

$$r(x) := \frac{d}{dx} H_m(x).$$

In 3D CSEM modelling, we apply the essentially non-oscillatory interpolation as follows. First, we interpolate the data in the in-line direction with the help of the primitive function. The results are then interpolated by the point-wise essentially non-oscillatory scheme in the two perpendicular directions.

We end this section by noting that the selection of the smoothest stencil by means of an if-statement may pose problems if the modelling code is used for least-squares inversion of electromagnetic measurements. Then, a differentiable version can be employed as proposed by van Albada, van Leer and Roberts (1982); see also Mulder and van Leer (1985).

APPENDIX B: THE VERTICAL COMPONENT IN THE THREE-LAYER PROBLEM

The vertical electric field component in the three-layer problem can be derived explicitly by solving equation (3) in the wave number domain and then taking the inverse Fourier transform to go back to the spatial domain (Ward and Hohmann 1987).

We consider a three-layer problem in an unbounded domain and number the top layer and the two layers below as 0, 1 and 2, respectively. Layer 1 has a thickness d. Each layer has different parameters, μ, ϵ and σ. A coordinate system is defined such that the origin is located at the interface of layer 0 and layer 1. A point source in the x-direction is placed at coordinate $(0, 0, z^s)$, $0 < z^s < d$.

Maxwell's equations for 1D layered media can be decomposed in either the horizontal electric and magnetic field components or the vertical electric and magnetic field components and their vertical derivatives. Both decomposition methods fully describe the total electromagnetic field. The latter method is of interest because the vertical electric field component is completely decoupled from the vertical magnetic field component. Here we are only interested in the vertical electric field and we choose to eliminate all horizontal components of the electromagnetic field. With this configuration, the vertical electric field component at a specific point $\mathbf{x} = (x, y, z)$ anywhere in the three-layered model is given by

$$E_z(\mathbf{x}, \omega) = \begin{cases} E_{z,0}(\mathbf{x}, \omega), & \text{for } z < 0; \\ E_{z,1}(\mathbf{x}, \omega), & \text{for } 0 < z < d; \\ E_{z,2}(\mathbf{x}, \omega), & \text{for } z > d \end{cases}$$

This expression is obtained by solving the following boundary value problem for the vertical electric field that is generated by a unit-strength x-directed electric current dipole source with an impulsive time-signature:

$$\tilde{E}_{z,0} = \tilde{A}_0^- \exp(\Gamma_0 z), \quad \text{for } z < 0, \tag{B1}$$

$$\tilde{E}_{z,1} = \frac{\mathrm{i}k_x}{2\eta_1} \mathrm{sign}(z - z^S) \exp(-\Gamma_1 |z - z^S|) + \tilde{A}_1^+ \exp(-\Gamma_1 z) + \tilde{A}_1^- \exp[-\Gamma(d - z)], \quad \text{for } 0 < z < d, \tag{B2}$$

$$\tilde{E}_{z,2} = \tilde{A}_2^+ \exp[-\Gamma_2 (z - d)], \quad \text{for } z > d, \tag{B3}$$

where $\tilde{A}_i^+$ denotes the amplitude of the down-going field and $\tilde{A}_i^-$ of the upgoing field in layer i. The vertical wavenumber of layer i is denoted by Γ_i and given by

$$\Gamma_i = \sqrt{\kappa^2 - \mathrm{i}\omega\mu_0\eta_i}, \qquad \mathrm{Re}\,(\Gamma) \geq 0, \tag{B4}$$

where $\kappa^2 = k_x^2 + k_y^2$ and $\eta_i = \sigma_i - \mathrm{i}\omega\varepsilon_i$. The boundary conditions require the vertical electric current to be continuous and the vertical derivative of the vertical electric field to be continuous across any source-free interface with a discontinuity in the electric medium parameters. This leads to four conditions for the four unknown field amplitudes in the three layers, which problem can be solved for the up and down-going field amplitudes. We use the solution only for the field components in the lower two layers, which leads to

$$E_{z,1}(\mathbf{x}, \omega) = 3\frac{x(z - z^s)}{R^2}\left(\frac{1}{R^2} + \frac{\gamma_1}{R}\right)\frac{\exp(-\gamma_1 R)}{4\pi\tilde{\sigma}_1 R} + i\omega\mu_0 \frac{x(z - z^s)}{R^2}\frac{\exp(-\gamma_1)}{4\pi R}, + \frac{x}{2\pi r}\int_{\kappa=0}^{\infty} (\tilde{E}_1^+(\kappa, z, \omega) + \tilde{E}_1^-(\kappa, z, \omega)) J_1(\kappa r)\kappa^2\,\mathrm{d}\kappa,$$

$$E_{z,2}(\mathbf{x}, \omega) = \frac{x}{2\pi r}\int_{\kappa=0}^{\infty} \tilde{E}_2^+(\kappa, z, \omega) J_1(\kappa r)\kappa^2\,\mathrm{d}\kappa,$$

and

$$\tilde{E}_1^+(\kappa, z, \omega) = \frac{\exp\left[-\Gamma_1(z+z^s)\right] - r_1^{TM}\exp\left[-\Gamma_1(2d+z-z^s)\right]}{1+r_0^{TM}r_1^{TM}\exp(-2\Gamma_1 d)}\frac{r_0^{TM}}{2\tilde{\sigma}_1},$$

$$\tilde{E}_1^-(\kappa, z, \omega) = \frac{\exp\left[-\Gamma_1(2d-z-z^s)\right] + r_0^{TM}\exp\left[-\Gamma_1(2d-z+z^s)\right]}{1+r_0^{TM}r_1^{TM}\exp(-2\Gamma_1 d)}\frac{r_1^{TM}}{2\tilde{\sigma}_1},$$

$$\tilde{E}_2^+(\kappa, z, \omega) = \frac{\exp\left[-\Gamma_1(d-z^s)\right] + r_0^{TM}\exp\left[-\Gamma_1(d+z^s)\right]}{1+r_0^{TM}r_1^{TM}\exp(-2\Gamma_1 d)} \times \frac{\left(1+r_1^{TM}\right)}{2\tilde{\sigma}_2}\exp[-\Gamma_2(z-d)].$$

The radial distance in the horizontal plane is given by $r = \sqrt{x^2+y^2}$ and the total distance is given by $R = \sqrt{x^2+y^2+(z-z^s)^2}$. The quantities $\gamma_i = \sqrt{-\mathrm{i}\omega\mu_i\tilde{\sigma}_i}$, $\Gamma_i = \sqrt{\kappa^2 - \mathrm{i}\omega\mu_i\tilde{\sigma}_i}$, where $\tilde{\sigma}_i = \sigma_i - \mathrm{i}\omega\epsilon_i$.The reflection coefficients are given by

$$r_0^{TM} = \frac{\tilde{\sigma}_1\Gamma_0 - \tilde{\sigma}_0\Gamma_1}{\tilde{\sigma}_1\Gamma_0 + \tilde{\sigma}_0\Gamma_1} \quad \text{and} \quad r_1^{TM} = \frac{\tilde{\sigma}_2\Gamma_1 - \tilde{\sigma}_1\Gamma_2}{\tilde{\sigma}_2\Gamma_1 + \tilde{\sigma}_1\Gamma_2}.$$

The two remaining Fourier-Bessel integrals are evaluated numerically using an adaptive 8-point Gauss quadrature for every receiver location separately.